

Laser Interaction with Surface in Powder Bed Melting Process and Its Impact on Temperature Profile, Bead and Melt Pool Geometry



Leila Ladani and Faiyaz Ahsan

Abstract Many researchers have focused on thermal, structural or other multi-physics modeling of laser and electron beam powder bed processes. However, in most cases, the laser heat source distribution is considered Gaussian as an ideal beam. However, power intensity distribution is a function of many parameters that need to be considered if realistic modeling of laser interaction with surface is desired. This work seeks to model the process in a more comprehensive and realistic manner by taking the laser physics into consideration including the wavelength, laser quality factor and laser beam parameter product. The model also uses a level set method to determine the shape of the bead and melt pool during melting and solidification process. Other physics including the heat transfer and fluid flow is incorporated in the simulation to model the whole process. This multiphysics process is used to model the melt pool geometry. Results are compared against an experiment for Inconel 718 alloy.

Keywords Non-Gaussian beams · Melt pool · Level set

Introduction

Powder bed metal additive manufacturing process is gaining increasing popularity due to its ability to create complex shaped metallic components. It is a process where three-dimensional metallic parts are produced layer by layer, which undergoes rapid heating, melting, solidification and cooling during the deposition process. In a powder bed process, a uniform bed of powder is first deposited on the substrate and then specific regions of the bed are melted by the laser beam.

L. Ladani (✉) · F. Ahsan
University of Texas at Arlington, Arlington, TX, USA
e-mail: leila.ladani@uta.edu; leila.j.ladani@gmail.com

F. Ahsan
e-mail: faiyaz.ahsan@mavs.uta.edu

© The Minerals, Metals & Materials Society 2019
The Minerals, Metals & Materials Society (ed.), *TMS 2019 148th Annual Meeting & Exhibition Supplemental Proceedings*, The Minerals, Metals & Materials Series, https://doi.org/10.1007/978-3-030-05861-6_29

This process can be achieved mainly in two ways: laser beam and electron beam. Laser and E-beam interaction with material are fundamentally different. Laser is an optical source, while E-beam is a beam made of energized electrons. In this study, mainly selective laser melting (SLM) will be discussed. In SLM, the powder particles absorb energy from the laser beam as it melts directly under the laser beam.

The literature on thermal modeling of powder bed processes is getting richer by day as many researchers have focused on this area. Since the process involves multiple physics, accurately modeling it also requires coupling of these physics in a multiphysics modeling approach or using other engineering techniques and approaches. Modeling of the melt pool includes the thermal modeling as well as the fluid dynamic modeling to represent the Marangoni fluid flow inside the melt pool which affects the temperature distribution, melt pool size and the final microstructure. Including both of these effects is a challenging problem faced by many researchers in the field.

To overcome the challenge of modeling both the thermal aspect as well as the fluid dynamic inside the melt pool, Romano et al. [1] introduced an approach in which an effective conduction coefficient for molten metal was used to account for the Marangoni effect due to the melt pool dynamic. Introduction of the effective liquid conductivity provided much closer results to the experimental values. Roberts et al. [2], Manvatkar et al. [3], He et al. [4], Heigel et al. [5], Ladani et al. [6] and Romano et al. [7] used different techniques to model the whole process. Marangoni flow, which is induced between two fluid surfaces due to a temperature gradient in surface tension, plays an important role in the heat transfer within the melt pool. Andreotta et al. [8] modeled this flow by including mass and momentum balance equations.

The current study was done with Inconel 718 alloy, which mainly consists of nickel (50%) and chromium (20%). There are many simulation and experimental studies that deal with the use of Inconel alloys as additive manufacturing materials. Studies performed by Zhao et al. [9], Jia and Gu [10], Baufeld [11] explored the microstructural properties of additively manufactured Inconel 718 parts.

It is important to have an idea of the temperature profile generated as accurately as possible during powder bed process, which affects the melt pool geometry, which in turn has a significant influence in the microstructure of the final material. In the models provided in the literature review, the laser is represented by a moving Gaussian heat source that decays radially. Horak et al. [12] observed the laser-material interaction zone with a video camera recording and found out that the beam profile differed from the Gaussian profile. Chang et al. [13] used a modified equation of heat source in laser spot welding. In order to model the laser-material interaction properly, laser physics needs to be employed in an appropriate manner. This study was conducted in a more realistic manner where one can change the laser properties like wavelength, beam quality factor, etc. and observe the resulting build outcome. Marangoni flow was also modeled by coupling computational fluid dynamics with heat transfer module. Temperature distribution and melt pool geometry were observed from the resulting simulation. The temperature profile was compared to the temperature data obtained from Gaussian distribution model. Bead geometry, which dictates the

consistency of the build as well as the dimensional accuracy, was obtained using the temperature data, which was then compared with experimental results.

Laser Heat Source

The purpose of this study was to model the laser interaction with powder bed in a realistic manner. When the laser interacts with a material, the intensity distribution over the material is represented by a Gaussian distribution beam [14] as shown below:

$$I(x, y, z) = \frac{2P}{\pi * w(z)^2} * \exp\left[-\frac{2 * (x^2 + y^2)}{w(z)^2}\right] \tag{1}$$

$$w(z) = w_0 * \text{sqrt}\left[1 + \left(\frac{\lambda * z}{\pi * (w_0)^2}\right)^2\right] \tag{2}$$

Here, $w(z)$ is the beam radius at a depth z , w_0 is the beam waist radius, and λ is the laser wavelength. Beam waist radius is the smallest radius of the beam at the point of focus. This Gaussian beam is an ideal beam, which does not accurately represent the real life beam propagation. In particular, as the laser power increases the deviation of this equation from actual laser distribution increases significantly [15]. To address this problem, a new parameter M^2 is introduced, which is called the beam quality factor. For Gaussian beam, the value of M^2 is 1. For non-Gaussian beams, the value is higher than one. This beam quality factor is what separates the ideal Gaussian beam from a real non-Gaussian beam. It is defined as [16]

$$M^2 = \text{BPP} * \frac{\pi}{\lambda} \tag{3}$$

where BPP is “beam parameter product” and is the product of beam radius (w_0) and the beam divergence half angle (θ). The laser used for the current study was a Yb-fiber with a wavelength of 1064 nm. To account for the beam quality factor, Eq. (2) can be rewritten as [15]:

$$w(z) = w_0 * \text{sqrt}\left[1 + \left(\frac{\lambda * z * M^2}{\pi * (w_0)^2}\right)^2\right] \tag{4}$$

which is the propagation equation for a real laser beam.

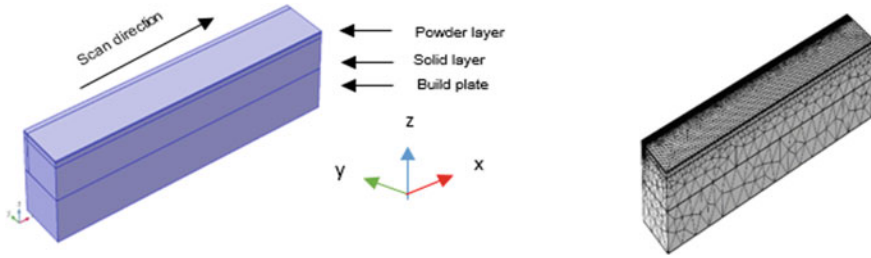


Fig. 1 Model setup and meshing

Modeling Technique

Comsol multiphysics software was used to generate the finite element model. This model was used to determine the temperature history of the build. The model consisted of three domains: build plate of 1 mm height upon which the process was completed, 0.9 mm of solidified part and powder domain at the top with a height of 0.4 mm which interacts with laser. The length and the width of all the domains were 9 mm and 3 mm, respectively. Planar symmetry was used in the geometry, and therefore only half of the melt pool and associated structure was modeled. Top surface was subject to radiation boundary loss to the environment. The side and bottom surfaces were kept insulated as the laser heat source is assumed to be highly localized phenomena. Figure 1 shows the model setup and the meshing of the model.

The governing equations used for energy, mass and moment are shown in the following equations:

$$\rho C_p \frac{\partial T}{\partial t} + \rho C_p \mathbf{u} \cdot \nabla T + \nabla \cdot \mathbf{q} = Q \tag{5}$$

$$\rho \frac{\partial \mathbf{u}}{\partial t} + \rho(\mathbf{u} \cdot \nabla)\mathbf{u} = \nabla \cdot [-p\mathbf{I} + \mu(\nabla\mathbf{u} + (\nabla\mathbf{u})^T)] + F \tag{6}$$

$$p \nabla(\mathbf{u}) = 0 \tag{7}$$

Equations (5), (6) and (7) represent energy, moment and mass balance, respectively. Here, \mathbf{u} is the velocity field, Q is the heat source, T is the temperature field, ρ is the density, C_p is the heat capacity, \mathbf{q} is the heat flux, μ is the dynamic viscosity, p is the pressure and \mathbf{I} is the identity matrix. Both fluid flow and thermal transport were modeled at the same time using these equations. Marangoni flow was used as a weak contribution with the following equation:

$$F = test(\mathbf{u}) \cdot \gamma \cdot T_x + test(\mathbf{v}) \cdot \gamma \cdot T_y \tag{8}$$

Table 1 Process parameters

| Process parameters | Values |
|------------------------|--------------------------|
| Laser wavelength (m) | 1.064 * 10 ⁻⁶ |
| Scan speed (mm/s) | 200, 700, 1200 |
| Laser power (W) | 100, 150, 200 |
| Beam radius (μm) | 100 |
| Penetration depth (μm) | 140 |
| Powder bed porosity | 0.3 |

which was added in Eq. (6). Here, γ is the surface tension coefficient, T_x and T_y are X- and Y-partial derivatives of temperature and u and v are the components of the velocity. The test functions turn differential equations into integral equations, which provide a numerical advantage.

The final mesh consisted of 126,609 (177252.6 nodes) tetrahedral elements, 38,989 triangular elements and 2680 edge elements and 292,856 number of degree of freedom in total. Higher density meshing was used around the melt pool region. Process parameters used for the modeling are stated in Table 1.

Material Properties

In this study, temperature-dependent properties were used to accurately model the whole process.

Temperature-dependent thermal conductivity of the powder materials was obtained experimentally with transient plane source (TPS-2200) instrument. TPS-2200 is an instrument used to measure the thermal properties of solid, liquid, paste and powder with high accuracy. The values of thermal conductivity acquired with a powder porosity of 0.3 were chosen for simulation purpose. Figure 2 shows thermal conductivity values for different packing densities.

Dynamic viscosity was calculated using the following equation [17]:

$$\mu(mPa * s) = .196e^{\frac{5848}{T}} \tag{9}$$

All the other material properties (heat capacity and density) were taken from mills [18].

Bead Geometry

For modeling the bead geometry, a two-dimensional local model was built (Fig. 3). The temperature history was acquired from the global model and imported into the local model. The location of the local model was selected where temperature is maximum. The local model was built with two domains, the molten pool region and

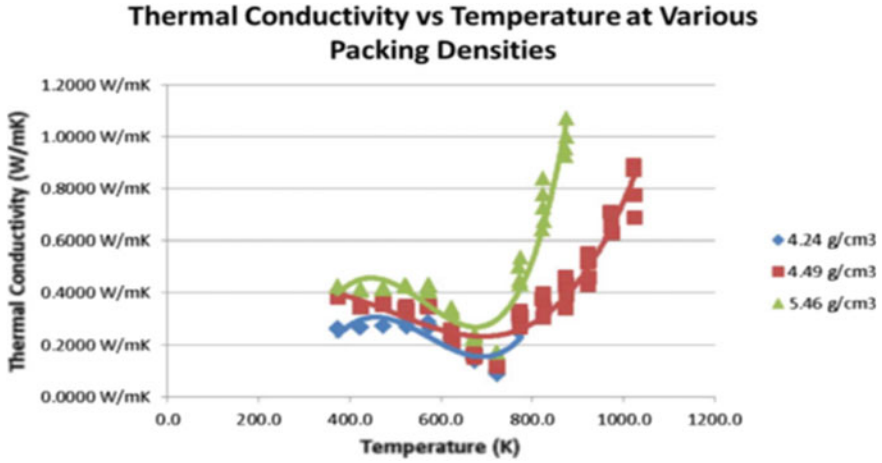


Fig. 2 TPS-2200 setup

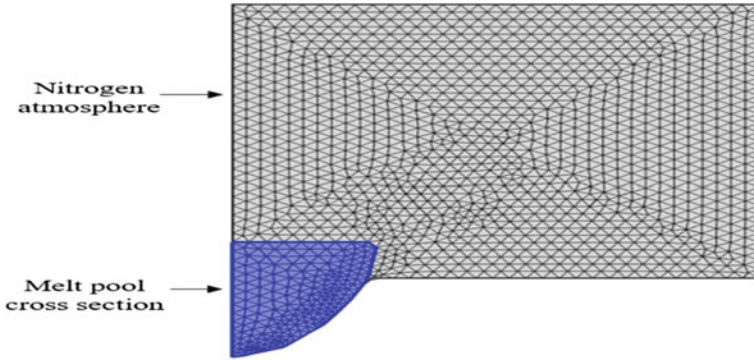


Fig. 3 Molten pool geometry

the outside atmosphere, which were separated by an interface. Then, level set method was used to track the interface of the molten pool and the nitrogen atmosphere to get the final bead geometry when the equilibrium was reached.

Level set method uses the following equations:

$$\nabla GI \cdot \nabla GI + \sigma_w \cdot GI (\nabla \cdot \nabla GI) = (1 + 2\sigma_w) GI^4 \tag{10}$$

$$\frac{\partial \emptyset}{\partial t} + \nabla \cdot (u\emptyset) = \lambda \nabla \cdot \left(\epsilon_{ls} \nabla \emptyset - \emptyset (1 - \emptyset) \frac{\nabla \emptyset}{|\nabla \emptyset|} \right) \tag{11}$$

Here, GI is the reciprocal interface distance, σ_w is the surface tension coefficient, u is the velocity field, λ is the reinitialization parameter, ϵ_{ls} is the parameter controlling interface thickness and \emptyset is the level set variable. For this model, $\sigma_w = 0.018$ N/m, $\lambda = 0.4$.

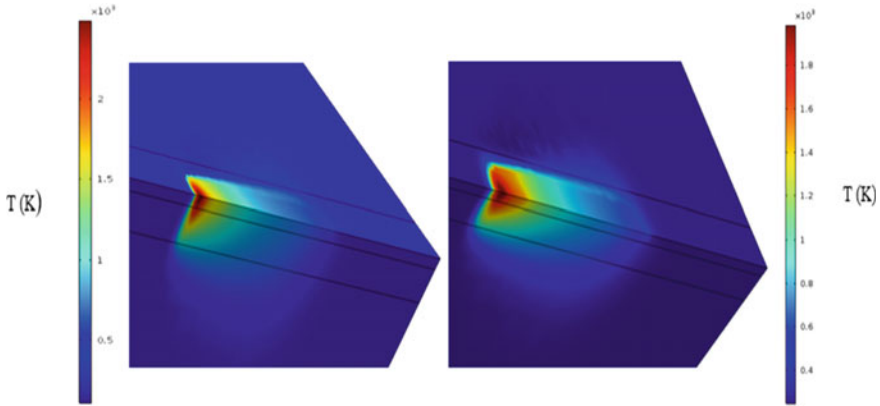


Fig. 4 Melt pool contour for **a** Gaussian and **b** non-Gaussian beam with scan speed = 200 mm/s and laser power = 100 W

Results and Discussion

Temperature Result

Figure 4 shows the melt pool profile of both the non-Gaussian and Gaussian beams. As it can be seen, the laser is more concentrated towards the center for the Gaussian beam. For the non-Gaussian beam, it deviates a bit compared to the Gaussian one. This result is expected as the quality of an ideal Gaussian beam is high; therefore, it is highly localized around the center of the beam. For a more realistic beam, as the beam quality factor M^2 increases, the quality of the beam starts to deteriorate as it reduces the focus of the beam. This is why, M^2 factor cannot be neglected while modeling the interaction of laser beam and material.

Figure 5 shows the temperature profile of Inconel 718 along the x-axis for Gaussian (G) and non-Gaussian (NG) beams with two different combinations of laser power and scan speed. For both combinations, temperature attains the maximum value for Gaussian model at the center of the beam. Again, this phenomenon is also apparent as the intensity will be higher for the more concentrated beam, i.e. the Gaussian one. As it can be observed, temperature profile is lower for 150 W/700 mm/s combination. Due to higher scan speed, the laser interacts with powder for a short period of time, so the intensity as well temperature decreases. For both of the combinations, temperature goes well above the melting temperature of Inconel 718, which is assumed to be 1443 K. Experimental temperature data for laser beam process could not be obtained from literature. However, it was observed that for electron beam process, the experimental temperature was much lower than that of Gaussian beam temperature [19]. In line with that, it can be stated that compared to the temperature profile obtained with Gaussian beam, the current study should be more similar to experimental temperature data.

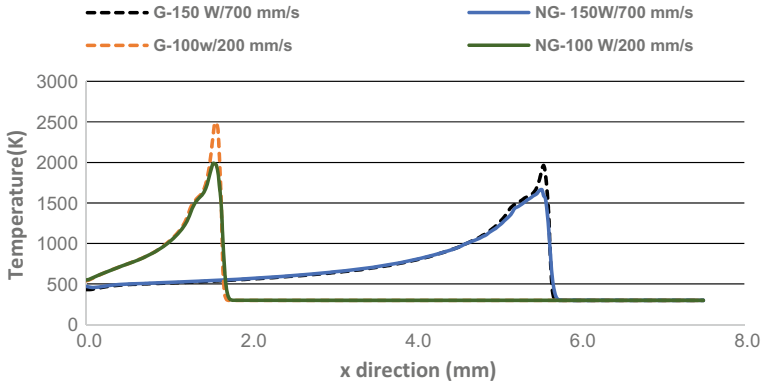


Fig. 5 Temperature along x-direction at time = 0.008 s

Bead Geometry

Table 2 shows a comparison of the bead geometry for non-Gaussian beam with M^2 factor, Gaussian beam and experimental results. Melt pool width, depth and bead height were compared.

As it can be seen, melt pool width results of non-Gaussian beams are more compatible than Gaussian beam results when compared with experimental results. The non-Gaussian beams generate lower maximum temperature when they interact with powder, which consequently results in smaller melt pool width than the Gaussian beam.

Bead height results obtained through experiment were limited as imperfections were found due to balling effect with the higher power/scan speed combinations. But, the trend observed for experimentally found bead heights was more similar to the non-Gaussian beam than Gaussian beam. So, it can be inferred that the result will follow the same trend for all the laser power/scan speed combinations.

As for the depth of melt pool, the results were not satisfactory. The melt pool depth of the Gaussian beam was better than non-Gaussian beam. Investigations are under way to understand these phenomena.

Table 2 Melt pool geometry

| | Non-Gaussian beam | | | Gaussian beam | | | Experimental results | | | Difference with experiment—Non Gaussian/Gaussian model | | |
|-----------------------------|-----------------------------|--------|--------|---------------|-------|--------------|----------------------|-------------|-------|--|---------------|--------------|
| | 100 W | 150 W | 200 W | 100 W | 150 W | 200 W | 100 W | 150 W | 200 W | 100 W | 150 W | 200 W |
| | <i>Melt pool width (µm)</i> | | | | | | | | | | | |
| 200 mm/s | 166.1 | 226.3 | | 184 | 231 | 154.2 ± 14.6 | 204 ± 11 | | | 12.9%/ 19.33% | 10.7%/ 13.07% | |
| 700 mm/s | | 122.5 | 134 | | 124 | 118 ± 5.0 | 144 ± 9.2 | | | 3.81%/ 5.08% | 7.26%/ 8.65% | |
| 1200 mm/s | | 109.12 | 117.02 | | 113 | 97 ± 8.1 | 113 ± 11.9 | | | 12.49%/ 16.49% | 3.01%/ 3.87% | |
| <i>Bead height (µm)</i> | | | | | | | | | | | | |
| 200 mm/s | 68 | 89 | | 60 | 77 | | 80 | 140 | | | 15%/ 25% | 36%/ 45% |
| 700 mm/s | | 70.2 | 73.5 | | 42 | 62 | | | | | | |
| 1200 mm/s | | 61 | | | 58 | | | | | | | |
| <i>Melt pool depth (µm)</i> | | | | | | | | | | | | |
| 200 mm/s | 74.5 | 108 | | 87 | 115 | 148.1 ± 40.3 | 215.7 ± 67.5 | | | 49.69%/ 41.26% | 49.9%/ 46.69% | |
| 700 mm/s | | 36 | 52.8 | | 42 | 60 | 48.2 ± 11.3 | 64.4 ± 18.2 | | | 25.3%/ 12.86% | 18.2%/ 6.83% |
| 1200 mm/s | | 9 | | | 10.5 | | 34.3 ± 14.2 | | | | 73.7%/ 69.12% | |

Conclusion

A three-dimensional thermal model was generated to determine the temperature profile of a non-Gaussian beam. The maximum temperature generated for non-Gaussian beam was lower than the maximum temperature of Gaussian beam due to lower beam quality. This temperature data was used to get the melt pool geometry for a more realistic non-Gaussian beam. Comparison of the melt pool width and the bead height with experiment shows a better correlation with non-Gaussian beam than Gaussian beam.

Acknowledgements The authors would like to express their deepest gratitude to Richard Andreotta for his immense contribution to this research.

References

1. Romano J, Ladani L, Sadowski M (2016) Laser additive melting and solidification of Inconel 718: finite element simulation and experiment. *JOM* 68(3):967–977
2. Roberts IA, Wang CJ, Esterlein R, Stanford M, Mynors DJ (2009) A three-dimensional finite element analysis of the temperature field during laser melting of metal powders in additive layer manufacturing. *Int J Mach Tools Manuf* 49(12–13):916–923
3. Manvatkar V, De A, Debroy T (2014) Heat transfer and material flow during laser assisted multi-layer additive manufacturing. *J Appl Phys* 116(12)
4. He X, Mazumder J (2007) Transport phenomena during direct metal deposition. *J Appl Phys* 101(5)
5. Heigel JC, Michaleris P, Reutzel EW (2015) Thermo-mechanical model development and validation of directed energy deposition additive manufacturing of Ti-6Al-4V. *Addit Manuf* 5:9–19
6. Ladani L, Romano J, Brindley W, Burlatsky S (2017) Effective liquid conductivity for improved simulation of thermal transport in laser beam melting powder bed technology. *Addit Manuf* 14:13–23
7. Romano J, Ladani L, Sadowski M (2015) Thermal modeling of laser based additive manufacturing processes within common materials. *Procedia Manuf* 1:238–250
8. Andreotta R, Ladani L, Brindley W (2017) Finite element simulation of laser additive melting and solidification of Inconel 718 with experimentally tested thermal properties. *Finite Elem Anal Des* 135:36–43
9. Zhao X, Chen J, Lin X, Huang W (2008) Study on microstructure and mechanical properties of laser rapid forming Inconel 718. *Mater Sci Eng A* 478(1–2):119–124
10. Jia Q, Gu D (2014) Selective laser melting additive manufacturing of Inconel 718 superalloy parts: densification, microstructure and properties. *J. Alloys Compd* 585:713–721
11. Baufeld B (2012) Mechanical properties of INCONEL 718 parts manufactured by shaped metal deposition (SMD). *J Mater Eng Perform* 21(7):1416–1421
12. Horak J, Heunoske D, Lueck M, Osterholz J, Wickert M (2015) Numerical modeling and characterization of the laser-matter interaction during high-power continuous wave laser perforation of thin metal plates. *J Laser Appl* 27:2015
13. Chang WS, NA SJ (2002) A study on heat source equations for the prediction of weld shape and thermal deformation in laser microwelding. *Metall Mater Trans B* 33(5):757–764
14. Li WB, Engström H, Powell J, Tan Z, Magnusson C (1996) *Lasers Eng* 5:175–183
15. Tobergte DR et al (2010) Gaussian beam optics. *Science* (80) 5(9):aae0330

16. Lasers and laser-related equipment—test methods for laser beam widths, divergence angles and beam propagation ratios (2005) [Online]. <https://www.iso.org/obp/ui/#iso:std:iso:11146:-1:ed-1:v1:en>
17. Brooks RF, Day AP, Andon RJL, Chapman LA, Mills KC, Queded PN (2001) Measurement of viscosities of metals and alloys with an oscillating viscometer. *High Temp-High Press* 33(1):73–82
18. Front Matter. *Recomm Values Thermophys Prop Sel Commer Alloy iii* (2002)
19. Romano J, Ladani L, Razmi J, Sadowski M (2015) Temperature distribution and melt geometry in laser and electron-beam melting processes—a comparison among common materials. *Addit Manuf* 8:1–11